ACS Catalysis

Research Article

pubs.acs.org/acscatalysis

Computational Insights into Oxygen Reduction Reaction and Initial Li_2O_2 Nucleation on Pristine and N-Doped Graphene in Li−O_2 Batteries

Yu Jing and Zhen Zhou*

Tianjin Key Laboratory of Metal and Molecule Based Material Chemistry, Key Laboratory of Advanced Energy Materials Chemistry (Ministry of Education), Computational Centre for Molecular Science, Institute of New Energy Material Chemistry, School of Materials Science and Engineering, Collaborative Innovation Center of Chemical Science and Engineering (Tianjin), Nankai University, Tianjin 300071, People's Republic of China

Supporting Information

ABSTRACT: Li−O_2 batteries have been a subject of extensive studies in the past few decades. However, the oxygen reduction reaction (ORR) mechanism is still unclear on air cathodes and needs to be concretely explored. In this work, by means of density functional theory computations, we systematically investigated the ORR and initial Li_2O_2 nucleation processes on the surface of pristine and N-doped graphene in Li−O_2 batteries. The in-plane pyridinic N-doped graphene is more effective in facilitating the nucleation of Li_2O_2 clusters than pristine or graphitic N-doped graphene. The overpotential of the rate-controlling step for Li_2O_2 nucleation decreases with the growth of Li_2O_2 clusters, and the cluster growth after $(Li_2O_2)_2$ will follow the process Li → LiO_2 → Li_2O_2 on all considered substrates. Our results should promote the understanding of ORR processes on N-doped graphene catalysts and shed more light on the design and optimization of air cathodes for Li−O_2 batteries.

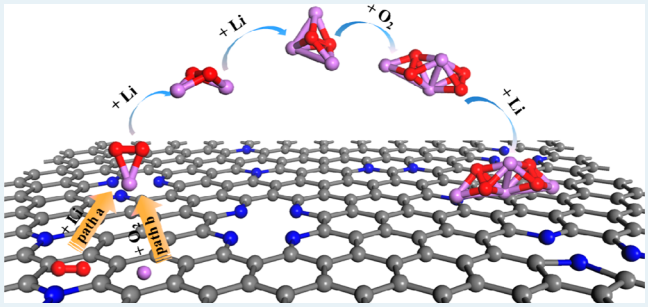

KEYWORDS: *N-doped graphene, ORR, air cathodes, Li−O_2 batteries, Li_2O_2*

1. INTRODUCTION

Thanks to the fast development of hybrid electric vehicles (EVs) and pure EVs, consumption of fossil fuels and CO_2 emission should be effectively reduced. However, the development of EVs is currently slowed by the limited gravimetric and volumetric energy density in available batteries. In comparison with all other battery chemistries, Li−O_2 batteries, first demonstrated by Abraham and Jiang,[1] exhibit much higher theoretical specific energy density (up to ∼3400 Wh/kg) and rather strong potency for powering EVs.[2] Since the investigations of Li−O_2 batteries are at their very beginning, many problems and challenges lie ahead before their commercial adoption, including poor cyclability and low energy efficiency.[3−5]

In order to improve the electrochemical performances of Li−O_2 batteries, many efforts have been devoted to exploring appropriate air cathode catalysts, which could effectively accelerate the oxygen reduction reaction (ORR) during discharging and the oxygen evolution reaction (OER) during charging. Among these proposed cathode catalysts, including but not limited to precious metals (Pt, Au, and Ru),[6−10] transition-metal oxides (MnO_2, Mn_3O_4, and Co_3O_4),[11−18] and carbon materials (carbon black, carbon nanotubes (CNTs), and graphene),[3,19−22] N-doped graphene is very attractive for the activation of the ORR due to low cost, high electronic conductivity, large surface area, and abundant surface defects.[23,24] Many experimental studies have demonstrated the good performance of N-doped graphene as a cathode catalyst for Li−O_2 batteries. For example, from a graphitization process of heteroatom polymers using CNTs as the templates, Wu et al. prepared N-doped graphene catalysts for Li−O_2 batteries, which exhibited electrocatalytic ability comparable to that of Pt cathodes.[25] The improved activity of N-doped graphene toward the ORR in nonaqueous Li−O_2 batteries was dominantly ascribed to the pyridinic N functionality. Recently, via a facile sol−gel route, Zhang et al. have prepared hierarchical carbon−nitrogen architectures as cathodes for Li−O_2 batteries.[26] The prepared carbon−nitrogen architectures showed great electrocatalytic activity and stable cyclability, due to the coexistence of active N sites on the carbon skeleton and favorable channels for Li^+ diffusion and electrolyte immersion in the hierarchical structure. However, due to the difficulty in tracing ORR/OER intermediates in experiments, the detailed mechanism of ORR/OER on the surface of N-doped graphene is still undetermined.

As a less limited approach, computations have become indispensable in accessing to the mechanism of ORR/OER for Li−O_2 batteries. Nørskov and co-workers first investigated the reactions at the cathode of an aprotic Li−O_2 battery by

Received: February 15, 2015
Revised: April 8, 2015
Published: June 3, 2015

DOI: 10.1021/acscatal.5b00332
ACS Catal. 2015, 5, 4309−4317

simulating the ORR on an $Li_2O_2(100)$ surface via density functional theory (DFT) computations.[27] They revealed the ORR mechanism by estimating the free energy of different intermediates and established possible origins of overpotential in discharge processes. Ceder and co-workers investigated the OER on the low-index surfaces of Li_2O_2 and found that the evolution of O_2 was the rate-determining step of the OER.[28] On the basis of their results, researchers conducted more studies to further explore the ORR/OER mechanisms on different cathode surfaces, such as Au(111), Pt(111),[29] $Co_3O_4(111)$,[30] and TiC(111).[31] In spite of those computational efforts to ORR/OER processes and Li_2O_2 properties in Li−O_2 batteries,[32−41] few studies have ever interpreted the reactions on the surface of catalytic cathodes. Since the discharging product Li_2O_2 cannot dissolve in the electrolyte in nonaqueous Li−O_2 batteries, Li_2O_2 will accumulate on the surface of cathodes with the progress of the ORR.[4,26] Therefore, the ORR in nonaqueous Li−O_2 batteries is simultaneously accompanied by the growth of Li_2O_2 on the surface of the cathodes. Thus, understanding the initial Li_2O_2 nucleation is an essential stage for understanding the ORR mechanism in Li−O_2 batteries.

In this work, we systematically investigated the initial ORR processes on the surface of N-doped graphene in comparison to those on pristine graphene, on the basis of DFT computations. Two possible paths (path a, $O_2 \rightarrow LiO_2 \rightarrow Li_2O_2$; path b, $Li \rightarrow LiO_2 \rightarrow Li_2O_2$) were considered for the initial nucleation of Li_2O_2, represented by the first adsorption of O_2 or Li on the surface of graphene. By estimating the free energy change of different intermediates, we predicted the preferred ORR processes at different sites of N-doped graphene. Among all the considered N-doped defects, pyridinic N exhibited the smallest overpotential in the initial ORR processes. The increasing charge transfer from Li_2O_2 clusters to different catalysts contributes to gradually enhanced Li adsorption with the progress of the ORR. Meanwhile, the overpotential of the controlling step decreases with the growth of Li_2O_2 clusters; thus, the ORR process will proceed favorably by steps. Our computations should shed more light on a better understanding of the ORR mechanism and help in screening effective catalysts for Li−O_2 batteries.

2. COMPUTATIONAL DETAILS

DFT computations were performed on the basis of the plane-wave technique implemented in the Vienna ab initio simulation package (VASP).[42] A projector-augmented plane wave (PAW) approach was used to describe the ion−electron interaction.[43,44] A generalized gradient approximation (GGA) expressed by the PBE (the abbreviation of the functional of Perdew, Burke, and Ernzerhof) functional[45] and a 400 eV cutoff for the plane-wave basis set were adopted in all computations. Self-consistent-field (SCF) computations were conducted with a convergence criterion of 10^{-4} eV on the total energy and the electron density. N-doped graphene was simulated by replacing a C atom with N in a 5 × 5 supercell, expanding along the a and b directions (a = b = 12.3 Å). The vacuum space in the c direction was set to be 20 Å to avoid any interlayer interactions in all cases. Integrations over the Brillouin zones were sampled with a 4 × 4 × 1 mesh of uniformly spaced k points for N-doped graphene and a 4 × 4 × 4 mesh for Li and Li_2O_2 bulk. Bader charge population analysis was conducted to evaluate the atomic charge and electron transfer in different systems.[46] The diffusion barrier of Li or/and O_2 on different surfaces was computed by locating the transition states, which can be obtained by computing the minimum-energy path (MEP) for the Li/O_2 diffusion processes by using the nudged elastic band (NEB) method.[47,48] In order to ascertain the reliability of computations in 5 × 5 supercells, we repeated related computations for graphene in 6 × 6 supercells, and detailed results are shown in Table S1 and Figure S1 in the Supporting Information. Small differences between the results of 5 × 5 and 6 × 6 supercells guarantee the validity of the conclusions in this work.

The standard free energy of Li_2O_2 is calculated based on eq 1

$$\Delta G_f^\circ = G_{Li_2O_2(s)}^\circ - 2G_{Li(s)}^\circ - G_{O_2(g)}^\circ = \Delta E_t + \Delta E_{zpe} - T\Delta S \quad (1)$$

which includes the formation energy (ΔE_t) of Li_2O_2, zero point energy correction (ΔE_{zpe}) and the entropy of O_2 (ΔS) under standard conditions (T = 298 K). Details on the calculation of ΔG_f° are discussed in the Supporting Information. According to the Nernst equation, $U_0 = -\Delta G_f^\circ/ne$, the calculated equilibrium potential is 2.92 V, ∼0.04 V lower than the experimental value (2.96 V). The slight underestimation of the equilibrium potential can be ascribed to the inaccuracy of DFT in estimating the cohesive energy of O_2.[27,29] However, since we used the same cohesive energy value of O_2 to estimate the formation of Li_2O_2, the examined free energy of formation is comparable at the same standard and the predicted tendency is reliable. In this study, all the intermediates at different steps were considered in their most stable configurations.

3. RESULTS AND DISCUSSION

3.1. Geometric and Electronic Properties of Pristine and N-Doped Graphene. According to previous investigations of N-doped graphene, there are three kinds of in-plane N configurations in the lattice of graphene, including graphitic N, pyridinic N, and pyrrolic N.[49−56] As shown in Figure 1a, the graphitic N (graphN1) is built by replacing one C atom with a N atom in a 5 × 5 supercell, corresponding to an N content of 2.33 wt %. The length of the N−C bond is 1.411 Å, close to that of the C−C bond (1.421 Å) in graphene. However, the other two C−C bonds of the C atom bonded to N are slightly elongated to 1.415 Å due to the electron-withdrawing nature of N. Double graphitic N (graphN2) is also taken into account by replacing two C atoms with two N atoms, which represents an N content of 4.64 wt %. In order to study the effect of N contents on the nucleation of Li_2O_2, we placed the two N atoms in the same hexagon. There are three possible configurations for graphN2 (details in Figure S2 in the Supporting Information), while the meta position for N atoms (shown in Figure 1b) is more preferred experimentally.[53,57] Therefore, only graphN2 shown in Figure 1b was considered in the following investigations.

According to previous studies, in-plane pyridinic N and pyrrolic N usually appear in the formation of tri-N-substituted vacancies.[58−60] In light of this, tri-N pyridinic (pyriN3) is built accompanied by a vacancy defect, as shown in Figure 1c. The N−C bond length (1.338 Å) is shorter than those in graphN1 and graphN2, while the C−C bonds in the matrix are all elongated to different extents due to the presence of a vacancy, indicating the instability of this configuration. Another tri-N N-doped graphene with a pyrrolic-like N (pyrroN3) is built similarly (as shown in Figure 1d), in which one N is in a pentagon instead of a hexagon. Note that N in the pentagon is not a critically pyrrolic N,[61] and the other two N atoms in the

DOI: 10.1021/acscatal.5b00332
ACS Catal. 2015, 5, 4309−4317

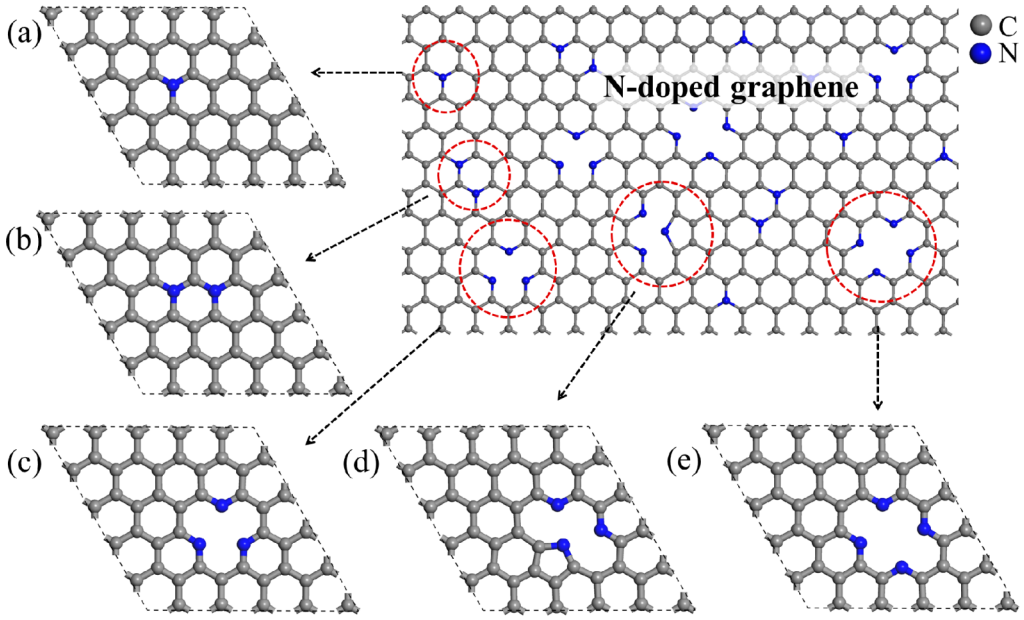

Figure 1. Schematic of N-doped graphene and structure models of (a) graphN1, (b) graphN2, (c) pyriN3, (d) pyrroN3, and (e) pyriN4.

Table 1. N Content, N−C Bond Length (L_{N-C}), E_f for Five N-Doped Graphene Configurations, and Charge Transfer from C to N (C/N) in graphN1, graphN2, pyriN3, pyrroN3, and pyriN4

	graphN1	graphN2	pyriN3	pyrroN3	pyriN4
N, wt %	2.33	4.64	7.07	7.07	9.59
L_{N-C}, Å	1.411	1.400/1.420	1.338	1.322/1.340/1.405	1.329/1.350
E_f, eV	+0.81	+1.96	+3.39	+5.63	+3.72
C/N, e	0.67	0.71	0.79	0.72/0.32	0.84

hexagon are both in fact pyridinic N. The N−C bond lengths in the hexagon are 1.322 and 1.340 Å, respectively, while the N−C bond lengths in the pentagons are about 1.405 Å. The N content is 7.07 wt % in both pyriN3 and pyrroN3. Meanwhile, in-plane tetra-N pyridinic (pyriN4) is also considered and corresponds to an N content of 9.59 wt %, as shown in Figure 1e. The N−C bonds in pyriN4 are 1.329 and 1.350 Å, respectively. Details for the N−C bonds and C−C bonds are provided in Figure S3a–f in the Supporting Information.

To estimate the stability of these N-doped graphene structures, we calculate their formation energy on the basis of eq 2

$$E_f = E_{NG} - n\mu_C - m\mu_N \quad (2)$$

where E_f is the calculated formation energy, E_{NG} represents the total energy of N-doped graphene, n and m represent the total number of C and N atoms, and μ_N and μ_C are the chemical potentials of C and N atoms, respectively. μ_C and μ_N are obtained from pristine graphene and nitrogen in the gas phase, respectively. The calculated formation energies for different N-doped graphene configurations are presented in Table 1. As calculated, graphN1 exhibits the smallest E_f of 0.81 eV, indicating its high feasibility to be available in experiments. With an increase in the N content, the E_f value of N-doped graphene increases except for the structures with the presence of N in pentagons. For example, pyrroN3 exhibits a much higher E_f value than other N-doped graphene structures, though it shares the same N content with pyriN3. This can be understood that, in pyrroN3, there is one N atom in a pentagon and the in-ring strain is stronger than that of the N-containing hexagons, as implied by the fact that the N−C bonds in a pentagon are longer than those in hexagons of pyrroN3 (as illustrated in Figure S3e in the Supporting Information). This indicates that the pyrrolic-like N in a pentagon is more unstable than the pyridinic N in a hexagon, and the preparation of pyrroN3 will be more difficult than that of other configurations for N-doped graphene.

The relative stability of different N-doped graphene configurations under real experimental conditions (N_2 gas environment) was further evaluated by comparing their Gibbs formation energy (ΔG_f) on the basis of eq 3[62]

$$\Delta G_f = E_f - \frac{m}{2}\mu_{N_2} \quad (3)$$

in which μ_{N_2} is a function of the temperature T and the partial N_2 gas pressure P, and can be expressed as

$$\mu_{N_2} = H^\circ(T) - H^\circ(0) - TS^\circ(T) + k_B T \ln\left(\frac{P}{P^\circ}\right) \quad (4)$$

where H° and S° are the enthalpy and entropy at the pressure P° = 1 bar, respectively. T = 298 K was adopted to compare the Gibbs formation energy of different N-doped graphene configurations. Thus, the curves of ΔG_f as a function of μ_{N_2} for different N-doped graphene configurations can be obtained and are shown in Figure 2. It is found that, at low μ_{N_2} values, graphN1 is more accessible in real experiments. At high μ_{N_2} values, it is easier to obtain pyriN4 than other N-doped graphene configurations. Therefore, at a certain temperature (T = 298 K), by controlling the N_2 concentration (corresponding to P), one can achieve graphN1 and pyriN4 alternately in an

DOI: 10.1021/acscatal.5b00332
ACS Catal. 2015, 5, 4309−4317

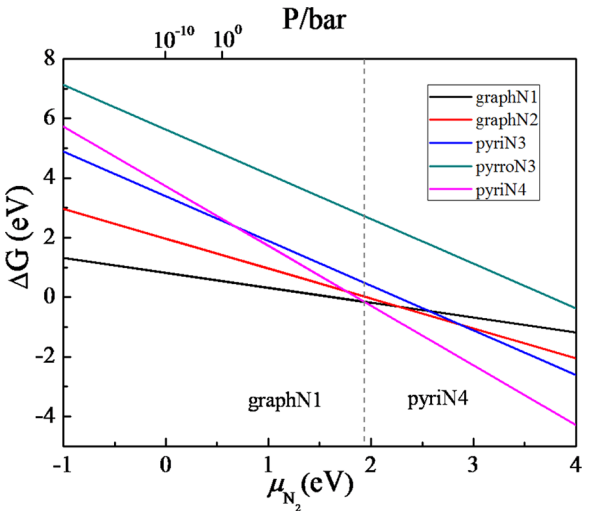

Figure 2. Gibbs formation energy (ΔG_f) as a function of chemical potential (μ_N) for different N-doped graphenes at 298 K. The dashed line divides the stability region.

N_2 gas environment. As demonstrated in previous studies,[51,63,64] the species and content of N in N-doped graphene can be tuned by controlling the preparation conditions (nitrogen source, temperature, and gas pressure).

To understand the N-doping effect on the electronic properties of graphene, we computed the partial density of states (PDOS) of different N-doped graphene configurations, as shown in Figure 3. The PDOS of graphene is also presented in Figure 3a for comparison. The valence and conduction band states of graphene touch each other at the Fermi level, exemplifying the zero-band-gap semiconducting character and "massless" carrier conduction behavior.

For N-doped graphene with graphitic N in both graphN1 and graphN2, the Fermi level moves up with energies of about +0.66 and +0.92 eV, respectively, as shown in Figure 3b,c. The upshift of Fermi level in graphN1 and graphN2 endows these two N-doped graphene configurations with n-type semiconducting and even metallic character.[63,65] The electron density isosurface of graphene (Figure S4a in the Supporting Information) shows uniform distribution of electron states on C atoms, while the electron density isosurfaces (Figure S4b,c in the Supporting Information) of graphN1 and graphN2 demonstrate the electron-rich states of N.

With respect to pyridinic N-doped graphene, a downshift in Fermi level happens to pyriN3, pyrroN3, and pyriN4, as shown in Figure 3d−f, with energies of about −0.60, −0.42, and −0.10 eV, respectively, indicating the p-type semiconducting character of these N-doped graphene configurations. The electron density isosurfaces shown in Figure S4d−f in the Supporting Information also identify the intense electron localization around N. In order to clarify the origin of p-type semiconducting character, we computed the PDOS of graphene with one C vacancy for comparison (Figure S5 in the Supporting Information), which also exhibits typical p-type semiconducting character. The p-type semiconducting character results from the fact that a carbon vacancy takes four valence electrons away, while three N atoms substituted for C atoms only bring three extra valence electrons in pyriN3 and pyrroN3, and two carbon vacancies take eight valence electrons away, while four N atoms only bring four extra valence electrons in pyriN4.

3.2. Initial Nucleation of Li_2O_2 on the Surface of Pristine and N-Doped Graphene. Next, we discuss the initial nucleation of Li_2O_2 on pristine and N-doped graphene by estimating the free energy change (ΔG) between different intermediates on different catalyst surfaces. For the initial ORR

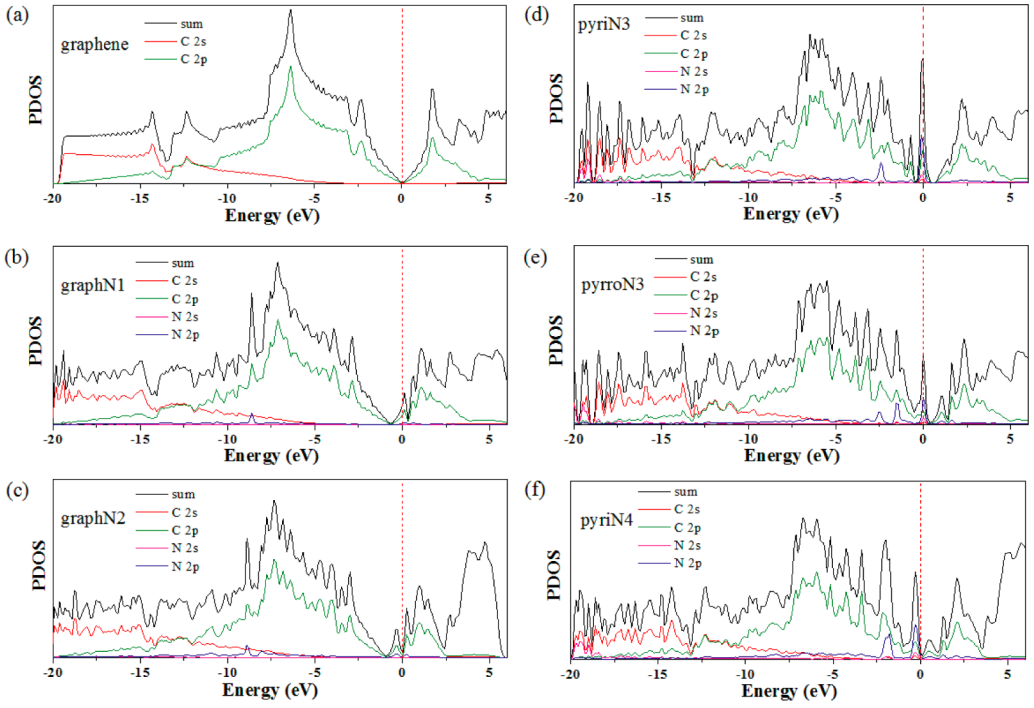

Figure 3. PDOS of (a) graphene, (b) graphN1, (c) graphN2, (d) pyriN3, (e) pyrroN3, and (f) pyriN4. The Fermi level is denoted with a red dashed line.

DOI: 10.1021/acscatal.5b00332
ACS Catal. 2015, 5, 4309−4317

Table 2. Adsorption Energy (E_{ads}) and Diffusion Barrier ($E_{barrier}$) of Li and O_2 on Pristine and N-Doped Graphene and the Rate-Determining Step (Step d) and Calculated Overpotential (η) for the Initial Li_2O_2 Nucleation on Different Substrates at U = 2.92 V

	graphene	graphN1	graphN2	pyriN3	pyrroN3	pyrriN4
E_{ads}(Li), eV	+0.10	+0.24	+0.34	−3.27	−2.75	−3.94
E_{ads}(O_2), eV	−0.09	−0.24	−0.34	−0.14	−0.15	−0.15
$E_{barrier}$(Li), eV	0.37	0.13	0.19	0.21	(0.17)	(0.18)
$E_{barrier}$(O_2), eV	0.01	0.00	0.06	0.04	0.002	0.07
step d	1st Li	1st Li	1st Li	2nd Li	2nd Li	2nd Li
η, V	1.40	1.58	1.67	1.30	0.95	1.23

processes on pristine and N-doped graphene, two possible reaction paths were considered here:

path a: $O_2 \rightarrow LiO_2 \rightarrow Li_2O_2$

path b: $Li \rightarrow LiO_2 \rightarrow Li_2O_2$

Path a is interpreted as the preferable adsorption of O_2, while path b represents the first adsorption of Li. To determine which path is preferred on pristine and N-doped graphene, we computed their adsorption energies for comparison. The adsorption energy of Li/O_2 is defined as

$$E_{abs} = E_{tot}(S+A) - E_{tot}(A) - E_{tot}(S) \quad (5)$$

where E_{tot}(S+A) is the DFT total energy of Li/O_2 adsorbed substrate, E_{tot}(A) is the total energy of Li(bulk) or O_2(gas), and E_{tot}(S) is the total energy of the free substrate.

Consistent with previous studies,[66,67] the electron-withdrawing N in N-doped graphene can stimulate its neighboring C atoms to be active sites for the adsorption of Li and O_2. The most stable adsorption configurations for Li and O_2 on different substrates can be found in Figure S6a−l in the Supporting Information. The calculated adsorption energies of Li and O_2 are presented in Table 2. The thermodynamic adsorptions of Li and O_2 differ with different substrates. Additionally, the adsorption of O_2 on pristine and N-doped graphene can also contribute to the decrease of magnetic moment of O_2 due to the interaction between O_2 and substrates (details in Table S2 in the Supporting Information). For graphene, graphN1, and graphN2, the adsorption of O_2 with negative E_{ads} value is thermodynamically more favorable than that of Li. Therefore, the initial ORR process on graphene, graphN1, and graphN2 will start with the adsorption of O_2 in path a. However, for pyriN3, pyrroN3, and pyriN4, the adsorption of Li is more preferable with large negative E_{ads} values, as shown in Table 2. Especially for pyrroN3 and pyriN4, when one Li is put on the hollow site neighboring the defect site (as illustrated in Figure S6i,k in the Supporting Information), it will spontaneously move to the defect site after full relaxation. The active defect site leads to cohesive bonds between Li and N and then drives these N-doped graphene structures to follow path b in the initial nucleation of Li_2O_2.

Since ion or molecule diffusion on electrodes can affect the electrochemical performances of batteries, we also computed the diffusion barrier of Li and O_2 on different substrates, as shown in Table 2. The kinetic diffusions of O_2 on these six substrates are all kinetically favorable with negligible barriers. The negligible diffusion barrier of O_2 on pristine and N-doped graphene is attributed to the physical adsorption of O_2 (more details are given in the Supporting Information). Although the diffusion barrier of Li is higher than that of O_2 on the surface of pristine and N-doped graphene, it is still small enough to facilitate effective electrochemical processes. In this respect, pristine and N-doped graphene are favorable for Li−O_2 batteries. The detailed diffusion path for Li and O_2 on pristine and N-doped graphene can be found in Figure S6 in the Supporting Information.

In order to further understand the nucleation of Li_2O_2 on different surfaces, the free energy change of different intermediary steps were then calculated on the basis of eq 6

$$\Delta G(n) = \Delta E_{tot}(n) + \Delta E_{zpe}(n) - T\Delta S(n) - eU \quad (6)$$

in which n represents the corresponding reaction step (n = 1, 2, 3, ...), while $\Delta E_{tot}(n)$, $\Delta E_{zpe}(n)$, and $T\Delta S(n)$ are the DFT total energy difference, zero point vibrational energy difference, and entropy change under standard conditions (T = 298 K) in step n, respectively.[68] The potential of a solvated Li^+ and an electron e in the electrode is set to be 0, in equilibrium with bulk Li.[27] Therefore, the free energy of an electron accompanying the adsorption of Li^+ essentially depends on the applied potential and will be shifted by $-eU$ under the potential of U.

As discussed above, the initial nucleation of Li_2O_2 on graphene, graphN1, and graphN2 follows path a, while ORR on pyriN3, pyrroN3, and pyrriN4 is initiated by path b. Details for the calculated $\Delta E_{tol}(n)$, $\Delta E_{zpe}(n)$, and $T\Delta S(n)$ in paths a and b for different catalysts can be found in Table S3 in the Supporting Information. Figure 4a shows the calculated free energy profiles for the initial nucleation of Li_2O_2 at an open circuit potential (U = 0 V). In both paths a and b for these six substrates, the O_2 adsorption step is always endothermic while the other two Li-containing steps are downhill in the free energy profiles. Therefore, the O_2 adsorption steps will be the kinetically controlling steps for Li_2O_2 nucleation in the open circuit case.

When applying the equilibrium potential (U = 2.92 V), as shown in Figure 4b, all the intermediary steps of the initial nucleation of Li_2O_2 become endothermic for graphene, graphN1, graphN2, and pyrroN3. In contrast, for pyriN3 and pyriN4, step 1 is downhill while steps 2 and 3 are uphill. In this case, the rate-determining step is no longer the O_2 adsorption but the Li-containing step. The overpotential (η) for the nucleation of Li_2O_2 on different surfaces can be obtained on the basis of the free energy change of the controlling step (ΔG_c), which is defined as $\eta = -\Delta G_c/e$. A lower η to overcome indicates an easier step to accomplish.

The controlling step and calculated η for different catalyst substrates can be found in Table 2. In the initial nucleation of Li_2O_2 under an equilibrium potential, the controlling step for graphene, graphN1, and graph2 is step 2, corresponding to the adsorption of the first Li^+ accompanied by the transfer of e^-; however, for pyriN3, pyrroN3, and pyriN4, the controlling step is step 3 , corresponding to the adsorption of the second Li^+ and e^-. Among these six catalysts, pyrroN3 exhibits the lowest

DOI: 10.1021/acscatal.5b00332
ACS Catal. 2015, 5, 4309−4317

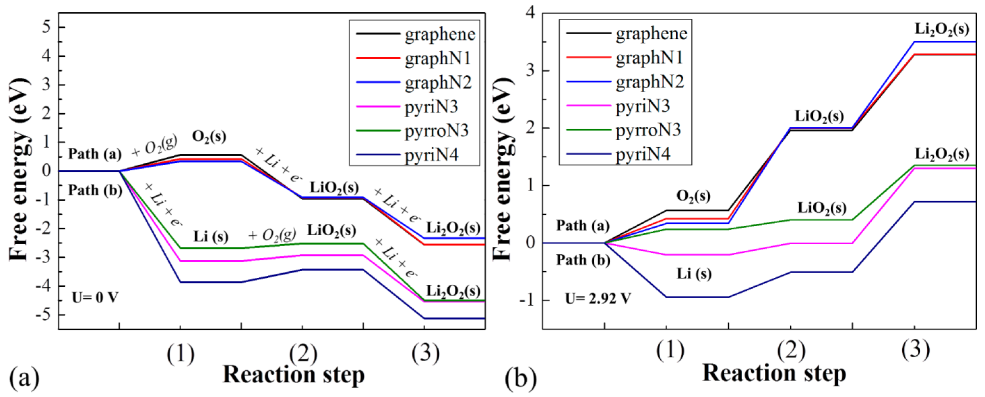

Figure 4. Calculated energetic profiles of the initial nucleation of Li_2O_2 on the surface of pristine and different N-doped graphenes at U = 0 V (a) and U = 2.92 V (b).

Table 3. Charge Transfer from Li_2O_2 (C/Li_2O_2) to Pristine and N-Doped Graphene Based on Bader Charge Analysis, the Substantial Adsorption Energies of Li or O_2 on Pristine and N-Doped Graphene with Nucleated Li_2O_2, Rate-Determining Step and Overpotential in the Substantial Nucleation of Li_4O_4 for Different Substrates, and Substantial Charge Transfer from Li_4O_4 (C/Li_4O_4) to Pristine and N-Doped Graphene

	graphene	graphN1	graphN2	pyriN3	pyrroN3	pyriN4
C/Li_2O_2, e	0.48	0.39	0.25	1.00	0.95	1.15
$E_{ads}(O_2)$ Li_2O_2, eV	−0.83	−0.89	−1.03	−0.61	−0.41	−0.61
E_{ads}(Li) Li_2O_2, eV	−1.70	−1.37	−1.31	−1.80	−1.80	−2.11
step d	1st Li	1st Li	1st Li	1st Li	1st Li	1st Li
η, V	1.25	1.56	1.66	1.17	1.14	0.89
C/Li_4O_4, e	0.62	0.54	0.47	1.06	1.07	1.47
E_{ads}(Li) Li_4O_4, eV	−1.98	−2.04	−1.96	−2.09	−2.34	−2.27

η value 0.95 V) while graphN2 shows the highest η value (1.67 V), and pyridinic N-doped graphene shows a lower η value than graphitic N-doped graphene. Since pyrroN3 is not easily accessible in experiments, as revealed in Figure 2, pyriN4 would be more applicable in catalyzing the initial nucleation of Li_2O_2.

The enhanced performance of pyridinic N-doped graphene toward catalyzing the initial Li_2O_2 nucleation can be ascribed to both N doping and the vacancy in the surface. Especially, the in-plane vacancy can act as strong electron-withdrawing sites, stabilize Li with high adsorption energy, and facilitate the nucleation of Li_2O_2 in path b. However, the strong adsorption of Li on pyridinic N-doped graphene generates a great obstacle for Li desorption in the reverse OER process. Therefore, it is predicted that the first adsorbed Li may not be released in the ultimate OER process of the first cycle but be stabilized in pyridinic N-doped graphene and work as a part of the catalyst in the following cycles.

3.3. Substantial Nucleation of Li_4O_4 on the Surface of Pristine and N-Doped Graphene. The substantial nucleation of Li_4O_4 on the surface of pristine and N-doped graphene was simulated after the formation of Li_2O_2, which can be regarded as the growth of Li_2O_2 clusters on different substrates. The charge transfer from the substrate to Li_2O_2 in different systems was first computed. As illustrated in Table 3, there is 0.48 e charge transfer from Li_2O_2 to graphene. As a comparison, Li_2O_2 donates less charge to graphN1 and graphN2 but contributes more charge to pyriN3, pyrroN3, and pyriN4. As a result, Li_2O_2 on graphN1 and graphN2 is more attractive to O_2 than the cases on pyriN3, pyrroN3, and pyriN4, while Li_2O_2 on pyriN3, pyrroN3, and pyriN4 is more attractive to Li than those on graphN1 and graphN2. However, after the formation of Li_2O_2, the adsorption of Li is stronger than that of O_2 for each substrate. Therefore, it is predicted that the substantial nucleation of Li_4O_4 will all follow path b in these six cases. The favorable adsorption of Li on Li_2O_2-anchored catalysts can be ascribed to the significant charge transfer from Li_2O_2 to the catalysts.

The nucleation of Li_4O_4 on different substrates was then simulated by measuring free energy changes of different intermediates according to eq 6. Detailed reaction steps and corresponding ΔE_{tol} (eV), ΔE_{zpe} (eV), and $T\Delta S$ (eV) values for the substantial nucleation of Li_4O_4 after Li_2O_2 on pristine and N-doped graphene can be found in Table S4 in the Supporting Information. As shown in Figure 5a, the energy profiles for the nucleation of Li_4O_4 were first explored when the applied voltage U is 0 V. For these six catalysts, all the three steps are exothermic and energetically favorable, except step 2 for pyriN4. The controlling step in the case of U = 0 V for all these six substrates is the adsorption of O_2 in step 2, corresponding to the formation of Li_3O_4.

When the applied voltage U is 2.92 V (shown in Figure 5b), all intermediary steps for these six systems are endothermic, except for the adsorption of O_2 on graphene, graphN1, graphN2, pyriN3, and pyrroN3. In this case, the controlling step is the Li-containing step instead of the O_2 adsorption step. The controlling step and overpotential for different substrates are shown in Table 3. The results demonstrate that the overpentential which can reflect the formation feasibility of Li_4O_4 on each substrate has been reduced in comparison with that of the nucleation of Li_2O_2. It is predicted that the overpotential will decrease gradually with the growth of Li_2O_2 clusters and finally approach the case of Li_2O_2 nucleation on the pure Li_2O_2 surface, which was explored in a previous study.[27] In comparison

DOI: 10.1021/acscatal.5b00332
ACS Catal. 2015, 5, 4309−4317

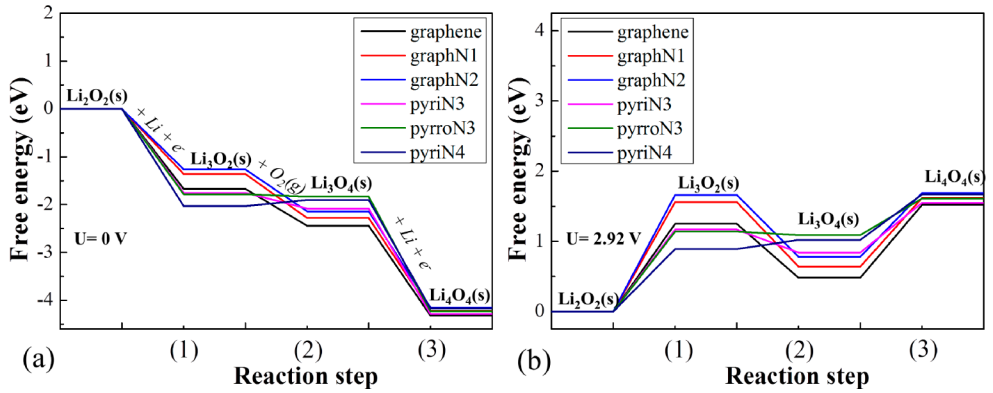

Figure 5. Energy profiles for the substantial nucleation of Li_4O_4 on different substrates under the potentials of U = 0 V (a) and U = 2.92 V (b).

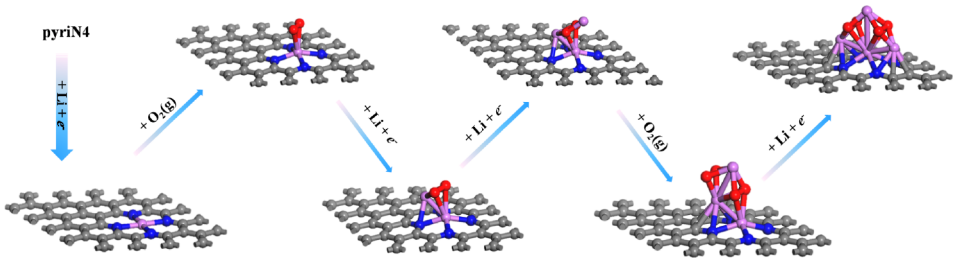

Figure 6. Schematics for the nucleation process of Li_4O_4 on the surface of pyriN4.

with graphene, pyriN3, pyrroN3, and pyriN4 exhibit lower overpotential and thus are more effective and favorable for the nucleation of Li_4O_4. On the other hand, graphN1 and graphN2 fail to effectively catalyze the nucleation of Li_4O_4. Therefore, in-plane pyridinic N is more effective than graphitic N in facilitating the initial nucleation of Li_2O_2. Moreover, pyriN4 exhibits the lowest η, as illustrated in Table 3, in comparison with pyriN3 and pyrroN3, which is very attractive for facilitating ORR. In view of the high accessibility of pyriN4 at higher N_2 gas pressure as indicated in Figure 2, we suggest that effective strategies can be adopted to enhance the content of pyriN4 in the preparation of N-doped graphene. In order to provide a visual illustration of the initial nucleation of Li_2O_2 on the surface of N-doped graphene, we provide the nucleation schematics of Li_2O_2 and then Li_4O_4 on the surface of pyriN4 (Figure 6).

After the nucleation of Li_4O_4, we further calculated the charge transfer between Li_4O_4 and catalysts. Table S5 in the Supporting Information shows a comparison for the charge transfer of each Li and O atom between Li_2O_2 and Li_4O_4 on the basis of Bader charge analysis, and substantial charge transfer from Li_4O_4 to pristine and N-doped graphene is also summarized in Table 3. As illustrated in Table 3, Li_4O_4 contributes increasing charge to the catalysts in comparison with Li_2O_2 and will be more attractive to Li in the substantial ORR. To verify this assumption, the adsorption of Li on Li_4O_4-supported catalysts is estimated and the E_{ads} value for each system is provided in Table 3. The results demonstrate that the pyridinic N-doped graphene still exhibits stronger Li adsorption than graphitic N-doped graphene, and the Li adsorption on Li_4O_4 is stronger than that on Li_2O_2. Therefore, we predict that path b will be much preferred in the following ORR after Li_4O_4 due to the increasing Li adsorption, and the favorable Li adsorption will contribute to the decrease of overpotentials.

Due to the significant potentials of in-plane pyridinic N-doped graphene toward catalyzing ORR in Li−O_2 batteries, pyriN4 is highly attractive in experiments. Especially, as implied in this study, pyriN4 can be selectively obtained in real experiments by using N_2 as the nitrogen source. Therefore, pyriN4, a low-cost and highly active cathode, is expected to be applied in Li−O_2 batteries in the near future. It is also predicted that cathodes with strong electron-withdrawing properties will tend to follow path b during ORR processes and can exhibit good ORR catalytic performances in Li−O_2 batteries.

4. CONCLUSIONS

In summary, pristine and N-doped graphene were selected as catalysts to computationally investigate the ORR and initial nucleation processes of Li_2O_2 in nonaqueous Li−O_2 batteries. Three types of N doping (graphitic N, pyridinic N, and pyrrolinic-like N) and five N contents (0−9.6 wt %) were involved in these six catalysts. The strong electron-withdrawing ability of N can cause its neighboring carbon to be active for the adsorption of Li/O_2, and meanwhile the vacancies associated with pyridinic N can trap Li.

Distinguished by the first adsorption of O_2 or Li, two paths (a, $O_2 \rightarrow LiO_2 \rightarrow Li_2O_2$; b, $Li \rightarrow LiO_2 \rightarrow Li_2O_2$) were proposed for the nucleation of Li_2O_2. The specific nucleation processes of Li_2O_2 and Li_4O_4 on pristine and N-doped graphene were interpreted by estimating the free energy of different intermediates under open circuit (U = 0 V) and equilibrium (U = 2.92 V) conditions, respectively. It is found that the charge transfer from the nucleated Li_2O_2 cluster to the carbon catalysts will increase with the growth of Li_2O_2 clusters. In the following ORR processes after Li_4O_4, path b will be more preferred due to the increasing adsorption of Li. Meanwhile, the overpotential of the controlling step will decrease with the growth of Li_2O_2 clusters and is predicted to approximate to the case of Li_2O_2 nucleation on a pure Li_2O_2 surface. As demonstrated, in-plane pyridinic N can reduce the overpotential of the controlling step more effectively than graphitic

DOI: 10.1021/acscatal.5b00332
ACS Catal. 2015, 5, 4309−4317

N and thus facilitate the nucleation of Li_2O_2. The enhanced catalytic properties of pyridinic N can be ascribed to the eletroton-withdrawing configurations, which lead to significant charge transfer from Li_2O_2 (Li_4O_4) to the substrates. However, the strong Li adsorption of in-plane pyridinic N would generate obstacles for the releases of Li in the reverse OER processes and the OER mechanism on N-doped graphene needs to be further explored in the future.

■ ASSOCIATED CONTENT

Supporting Information

The Supporting Information is available free of charge on the ACS Publications website at DOI: 10.1021/acscatal.5b00332.

Computational details and results (PDF)

■ AUTHOR INFORMATION

Corresponding Author

*E-mail for Z.Z.: zhouzhen@nankai.edu.cn.

Notes

The authors declare no competing financial interest.

■ ACKNOWLEDGMENTS

This work was supported by the Ph.D. Candidate Research Innovation Fund of Nankai University, NSFC (21473094 and 21421001), and MOE Innovation Team (IRT13022) in China.

■ REFERENCES

(1) Abraham, K.; Jiang, Z. *J. Electrochem. Soc.* **1996**, *143*, 1−5.
(2) Li, F.; Kitaura, H.; Zhou, H. *Energy Environ. Sci.* **2013**, *6*, 2302−2311.
(3) Li, F.; Zhang, T.; Zhou, H. *Energy Environ. Sci.* **2013**, *6*, 1125−1141.
(4) Shao, Y.; Ding, F.; Xiao, J.; Zhang, J.; Xu, W.; Park, S.; Zhang, J. G.; Wang, Y.; Liu, J. *Adv. Funct. Mater.* **2013**, *23*, 987−1004.
(5) Cheng, F.; Chen, J. *Chem. Soc. Rev.* **2012**, *41*, 2172−2192.
(6) Lim, H.-D.; Song, H.; Gwon, H.; Park, K.-Y.; Kim, J.; Bae, Y.; Kim, H.; Jung, S.-K.; Kim, T.; Kim, Y. H. *Energy Environ. Sci.* **2013**, *6*, 3570−3575.
(7) Lu, Y.-C.; Xu, Z.; Gasteiger, H. A.; Chen, S.; Hamad-Schifferli, K.; Shao-Horn, Y. *J. Am. Chem. Soc.* **2010**, *132*, 12170−12171.
(8) Peng, Z.; Freunberger, S. A.; Chen, Y.; Bruce, P. G. *Science* **2012**, *337*, 563−566.
(9) Li, F.; Tang, D.-M.; Chen, Y.; Golberg, D.; Kitaura, H.; Zhang, T.; Yamada, A.; Zhou, H. *Nano Lett.* **2013**, *13*, 4702−4707.
(10) Jung, H.-G.; Jeong, Y. S.; Park, J.-B.; Sun, Y.-K.; Scrosati, B.; Lee, Y. J. *ACS Nano* **2013**, *7*, 3532−3539.
(11) Débart, A.; Paterson, A. J.; Bao, J.; Bruce, P. G. *Angew. Chem., Int. Ed.* **2008**, *47*, 4521−4524.
(12) Débart, A.; Bao, J.; Armstrong, G.; Bruce, P. G. *J. Power Sources* **2007**, *174*, 1177−1182.
(13) Yu, Y.; Zhang, B.; He, Y.-B.; Huang, Z.-D.; Oh, S.-W.; Kim, J.-K. *J. Mater. Chem. A* **2013**, *1*, 1163−1170.
(14) Li, Q.; Xu, P.; Zhang, B.; Tsai, H.; Wang, J.; Wang, H.-L.; Wu, G. *Chem. Commun.* **2013**, *49*, 10838−10840.
(15) Zhang, H.; Qiao, H.; Wang, H.; Zhou, N.; Chen, J.; Tang, Y.; Li, J.; Huang, C. *Nanoscale* **2014**, *6*, 10235−10242.
(16) Sun, C.; Li, F.; Ma, C.; Wang, Y.; Ren, Y.; Yang, W.; Ma, Z.; Li, J.; Chen, Y.; Kim, Y. *J. Mater. Chem. A* **2014**, *2*, 7188−7196.
(17) Cui, Y.; Wen, Z.; Liu, Y. *Energy Environ. Sci.* **2011**, *4*, 4727−4734.
(18) Black, R.; Lee, J. H.; Adams, B.; Mims, C. A.; Nazar, L. F. *Angew. Chem., Int. Ed.* **2013**, *52*, 392−396.
(19) Gallant, B. M.; Mitchell, R. R.; Kwabi, D. G.; Zhou, J.; Zuin, L.; Thompson, C. V.; Shao-Horn, Y. *J. Phys. Chem. C* **2012**, *116*, 20800−20805.
(20) Yang, Z.; Yao, Z.; Li, G.; Fang, G.; Nie, H.; Liu, Z.; Zhou, X.; Chen, X.; Huang, S. *ACS Nano* **2011**, *6*, 205−211.
(21) Yoo, E.; Zhou, H. *ACS Nano* **2011**, *5*, 3020−3026.
(22) Jung, H.-G.; Hassoun, J.; Park, J.-B.; Sun, Y.-K.; Scrosati, B. *Nat. Chem.* **2012**, *4*, 579−585.
(23) Kong, X.-K.; Chen, C.-L.; Chen, Q.-W. *Chem. Soc. Rev.* **2014**, *43*, 2841−2857.
(24) Wang, H.; Maiyalagan, T.; Wang, X. *ACS Catal.* **2012**, *2*, 781−794.
(25) Wu, G.; Mack, N. H.; Gao, W.; Ma, S.; Zhong, R.; Han, J.; Baldwin, J. K.; Zelenay, P. *ACS Nano* **2012**, *6*, 9764−9776.
(26) Zhang, Z.; Bao, J.; He, C.; Chen, Y.; Wei, J.; Zhou, Z. *Adv. Funct. Mater.* **2014**, *24*, 6826−6833.
(27) Hummelshøj, J. S.; Blomqvist, J.; Datta, S.; Vegge, T.; Rossmeisl, J.; Thygesen, K. S.; Luntz, A. C.; Jacobsen, K. W.; Nørskov, J. K. *J. Chem. Phys.* **2010**, *132*, 071101.
(28) Mo, Y.; Ong, S. P.; Ceder, G. *Phys. Rev. B: Condens. Matter Mater. Phys.* **2011**, *84*, 205446.
(29) Xu, Y.; Shelton, W. A. *J. Chem. Phys.* **2010**, *133*, 024703.
(30) Zhu, J.; Ren, X.; Liu, J.; Zhang, W.; Wen, Z. *ACS Catal.* **2015**, *5*, 73−81.
(31) Wang, Z.; Sun, J.; Cheng, Y.; Niu, C. *J. Phys. Chem. Lett.* **2014**, *5*, 3919−3923.
(32) Yang, G.; Wang, Y.; Ma, Y. *J. Phys. Chem. Lett.* **2014**, *5*, 2516−2521.
(33) Radin, M. D.; Siegel, D. J. *Energy Environ. Sci.* **2013**, *6*, 2370−2379.
(34) Lau, K. C.; Curtiss, L. A.; Greeley, J. *J. Phys. Chem. C* **2011**, *115*, 23625−23633.
(35) Garcia-Lastra, J. M.; Myrdal, J.; Christensen, R.; Thygesen, K.; Vegge, T. *J. Phys. Chem. C* **2013**, *117*, 5568−5577.
(36) Radin, M. D.; Rodriguez, J. F.; Tian, F.; Siegel, D. J. *J. Am. Chem. Soc.* **2011**, *134*, 1093−1103.
(37) Black, R.; Oh, S. H.; Lee, J.-H.; Yim, T.; Adams, B.; Nazar, L. F. *J. Am. Chem. Soc.* **2012**, *134*, 2902−2905.
(38) Dunst, A.; Epp, V.; Hanzu, I.; Freunberger, S.; Wilkening, M. *Energy Environ. Sci.* **2014**, *7*, 2739−2752.
(39) Mekonnen, Y. S.; Knudsen, K. B.; Mýrdal, J. S.; Younesi, R.; Højberg, J.; Hjelm, J.; Norby, P.; Vegge, T. *J. Chem. Phys.* **2014**, *140*, 121101.
(40) Luntz, A. C.; Viswanathan, V.; Voss, J.; Varley, J. B.; Nørskov, J.; Scheffler, R.; Speidel, A. *J. Phys. Chem. Lett.* **2013**, *4*, 3494−3499.
(41) Yun, K.-H.; Hwang, Y.; Chung, Y.-C. *J. Power Sources* **2015**, *277*, 222−227.
(42) Kresse, G.; Hafner, J. *Phys. Rev. B: Condens. Matter Mater. Phys.* **1993**, *47*, 558−561.
(43) Blöchl, P. E. *Phys. Rev. B: Condens. Matter Mater. Phys.* **1994**, *50*, 17953−17979.
(44) Kresse, G.; Joubert, D. *Phys. Rev. B: Condens. Matter Mater. Phys.* **1999**, *59*, 1758−1775.
(45) Perdew, J. P.; Burke, K.; Ernzerhof, M. *Phys. Rev. Lett.* **1996**, *77*, 3865−3868.
(46) Henkelman, G.; Arnaldsson, A.; Jónsson, H. *Comput. Mater. Sci.* **2006**, *36*, 354−360.
(47) Henkelman, G.; Jonsson, H. *J. Chem. Phys.* **2000**, *113*, 9978−9985.
(48) Olsen, R.; Kroes, G.; Henkelman, G.; Arnaldsson, A.; Jónsson, H. *J. Chem. Phys.* **2004**, *121*, 9776−9792.
(49) Zhao, L.; He, R.; Rim, K. T.; Schiros, T.; Kim, K. S.; Zhou, H.; Gutiérrez, C.; Chockalingam, S.; Arguello, C. J.; Pálová, L. *Science* **2011**, *333*, 999−1003.
(50) Gao, H.; Song, L.; Guo, W.; Huang, L.; Yang, D.; Wang, F.; Zuo, Y.; Fan, X.; Liu, Z.; Gao, W. *Carbon* **2012**, *50*, 4476−4482.
(51) Zhang, S.; Tsuzuki, S.; Ueno, K.; Dokko, K.; Watanabe, M. *Angew. Chem., Int. Ed.* **2015**, *54*, 1302−1306.
(52) Zhang, S.; Dokko, K.; Watanabe, M. *Chem. Mater.* **2014**, *26*, 2915−2926.
(53) Deng, D.; Pan, X.; Yu, L.; Cui, Y.; Jiang, Y.; Qi, J.; Li, W.-X.; Fu, Q.; Ma, X.; Xue, Q. *Chem. Mater.* **2011**, *23*, 1188−1193.

DOI: 10.1021/acscatal.5b00332
ACS Catal. 2015, 5, 4309−4317

(54) Zhang, S.; Miran, M. S.; Ikoma, A.; Dokko, K.; Watanabe, M. *J. Am. Chem. Soc.* **2014**, *136*, 1690−1693.
(55) Zhang, L.-S.; Liang, X.-Q.; Song, W.-G.; Wu, Z.-Y. *Phys. Chem. Chem. Phys.* **2010**, *12*, 12055−12059.
(56) Panchakarla, L.; Subrahmanyam, K.; Saha, S.; Govindaraj, A.; Krishnamurthy, H.; Waghmare, U.; Rao, C. *Adv. Mater.* **2009**, *21*, 4726−4730.
(57) Lv, R.; Li, Q.; Botello-Méndez, A. R.; Hayashi, T.; Wang, B.; Berkdemir, A.; Hao, Q.; Elías, A. L.; Cruz-Silva, R.; Gutiérrez, H. R.; Kim, Y. A.; Muramatsu, H.; Zhu, J.; Endo, M.; Terrones, H.; Charlier, J.-C.; Pan, M.; Terrones, M. *Sci. Rep.* **2012**, *2*, 586.
(58) Yu, Y.-X. *Phys. Chem. Chem. Phys.* **2013**, *15*, 16819−16827.
(59) Ma, C.; Shao, X.; Cao, D. *J. Mater. Chem.* **2012**, *22*, 8911−8915.
(60) Rangel, E.; Magana, L. F.; Sansores, L. E. *ChemPhysChem* **2014**, *15*, 4042−4048.
(61) Pels, J.; Kapteijn, F.; Moulijn, J.; Zhu, Q.; Thomas, K. *Carbon* **1995**, *33*, 1641−1653.
(62) Li, Y.; Zhou, Z.; Cabrera, C. R.; Chen, Z. *Sci. Rep.* **2013**, *3*, 2030.
(63) Usachov, D.; Fedorov, A.; Vilkov, O.; Senkovskiy, B.; Adamchuk, V. K.; Yashina, L. V.; Volykhov, A. A.; Farjam, M.; Verbitskiy, N. I.; Grüneis, A. *Nano Lett.* **2014**, *14*, 4982−4988.
(64) Shi, Z.; Kutana, A.; Yakobson, B. I. *J. Phys. Chem. Lett.* **2015**, *6*, 106−112.
(65) Muhich, C. L.; Westcott, J. Y., IV; Morris, T. C.; Weimer, A. W.; Musgrave, C. B. *J. Phys. Chem. C* **2013**, *117*, 10523−10535.
(66) Gao, Y.; Hu, G.; Zhong, J.; Shi, Z.; Zhu, Y.; Su, D. S.; Wang, J.; Bao, X.; Ma, D. *Angew. Chem., Int. Ed.* **2013**, *52*, 2109−2113.
(67) Yan, H.; Xu, B.; Shi, S.; Ouyang, C. *J. Appl. Phys.* **2012**, *112*, 104316.
(68) Hwang, Y.; Yun, K.-H.; Chung, Y.-C. *J. Power Sources* **2015**, *275*, 32−37.

DOI: 10.1021/acscatal.5b00332
ACS Catal. 2015, 5, 4309−4317